Simultaneous Positioning and Orientation of a Single Nano-Object by Flow Control: Theory and Simulations

Pramod P. Mathai [1], Andrew J. Berglund [2], J. Alexander Liddle [2], and Benjamin A. Shapiro [3]

1. Joint appointment with Center for Nanoscale Science and Technology (CNST) at the National Institute of Standards and Technology (NIST), Gaithersburg, MD-20899 USA and Institute for research in electronics and applied physics, University of Maryland (UMD), College Park, MD-20742, USA.

E-mail: pramod.mathai@nist.gov
2. CNST,NIST
3. Department of Bioengineering, UMD

Abstract. In this paper we theoretically describe a method to simultaneously control both the position and orientation of single nano-objects in fluids by precisely controlling the flow around them. We develop and simulate a control law that uses electro-osmotic flow (EOF) actuation to translate and rotate rigid nano-objects in two spatial dimensions. Using EOF to control nano-objects offers advantages as compared to other approaches: a wide class of objects can be manipulated (no magnetic or electric dipole moments are needed), the object can be controlled over a long range (> 100 μm) with sub-micrometer accuracy, and control may be achieved with simple polydimethylsiloxane (PDMS) devices. We demonstrate the theory and numerical solutions that will enable deterministic control of the position and orientation of a nano-object in solution, which can be used, for example, to integrate nanostructures in circuits and orient sensors to probe living cells.

1. Introduction

We theoretically describe a technique for simultaneously positioning and orienting single nano-objects in a fluid in two spatial dimensions by manipulating the flow around them. We address two object control goals with this technique. The first is the ability to move the object across large distances (tens of micrometers). The second is the ability to accurately control the position and orientation of objects of a variety of shapes and material properties - for example, semiconductors [1], conductors [2], and dielectrics [3].

Previously, we showed simulations demonstrating *position* control of *spherical* objects [4] in a microfluidic device using electro-osmotic flow (EOF) control. The ideas developed in that study enabled an experimental demonstration of position control of micrometer sized spherical objects to sub-micrometer accuracy [5] and subsequently the

control of nanoscopic particles (single quantum dots) to nanometer precision [6]. In this paper, we explain and simulate a technique that shows how the translational and *shear* components of the flow field in the device can be manipulated, to trap an object at a desired position and orientation or manipulate both its position and orientation along a desired trajectory.

Existing approaches for simultaneously controlling the position and orientation of a single (or a few) object(s) can be classified into actuation strategies that include optical, magnetic, and electrical techniques. If objects have a higher refractive index than their surrounding medium, a laser beam can be used to attract the object into the region of highest light intensity. Variations of this basic principle have been used to transfer translational and angular momentum from the laser beam to the object by either making use of special optical properties of the object or by manipulating the wave front of the incident light [7, 8, 9, 10, 11, 12, 13].

Magnetic fields in combination with fluidic forces have been used to control magnetic objects [14], or with a combination of optical forcing for translation and electromagnets for rotation [15]. Apart from the requirement that the object be magnetic, the objects may require specially designed shapes to enable fluidic actuation [16]. Alternatively, magnetic features are lithographically patterned on objects to allow manipulation of their orientation by magnetic fields [17].

If the object has a significant dipole moment, dielectrophoresis (a type of electric actuation) can be used to position and orient nanowires [18, 19, 20, 21, 22, 23] and biological cells [24]. In this technique a high electric field gradient interacts with the object's dipole moment to translate and rotate the object. Since the electric field gradients have to be high, the object is controlled near an electrode in a device where the gradient is steep.

The position and orientation control that we present below uses electrical actuation to modulate the flow around an object. Our technique depends on controlling viscous drag, a force that applies to every object, and can hence be used to control a general class of object - the object does not have to be charged or magnetic or have any other special properties. Our simulations will show that the object can be controlled across a large (≈ 100 μm) region. The approach uses feedback control of shear flow in a microfluidic device to translate and rotate the object. The fluidic shear force acting on the object (which is assumed to be inertia-less) suspended in the fluid, rotates the object to any desired orientation (left panel of Fig. 1) while the translational component of the fluidic drag moves it to any desired location in a 2-dimensional control region. The position and orientation of the object, which are randomly perturbed due to Brownian motion, are measured at regular intervals. From this visual measurement, a feedback control loop determines and applies the fluid flow that will translate and rotate the object from where it is towards where it should be (see right panel of Fig. 1).

The flow is actuated electro-osmotically. Here the electric field moves the fluid which moves the object by viscous forces [25, 26] (which is different from electrophoretic or dielectrophoretic actuation where the electric field creates a force directly on a charged

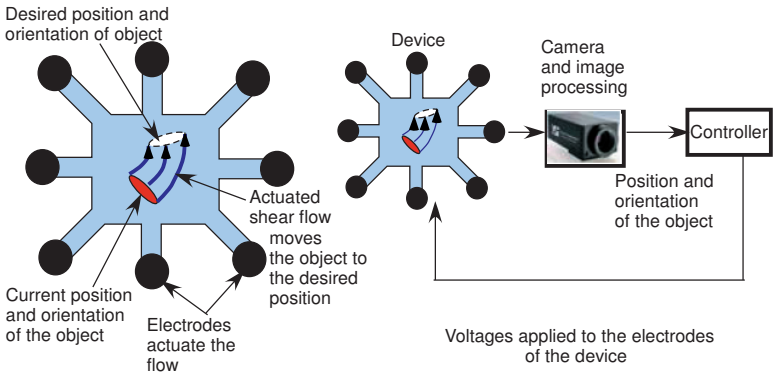

Figure 1. The left panel shows a schematic of the top view of the proposed device. The electrodes actuate a flow that translates and rotates the object from its current to its desired position and orientation. The right panel shows the feedback loop that achieves flow control in the device. At every instant, a camera captures an image of the object and an image processing algorithm computes the position and orientation of the object and transmits that information to the controller. The controller uses this information to actuate a flow in the device (by creating an electric field that moves the fluid in the device) that translates and rotates the object to the desired position and orientation.

or polarizable object). By using multiple (here 8) electrodes in concert (see Fig.2) it is possible to create complex electric field patterns in space, and in our thin planar devices those patterns are faithfully transmitted to the fluid flow in the control region. Feedback control of those patterns in time has allowed us to control the position of single objects [6], and is here being extended to also allow control of their orientation.

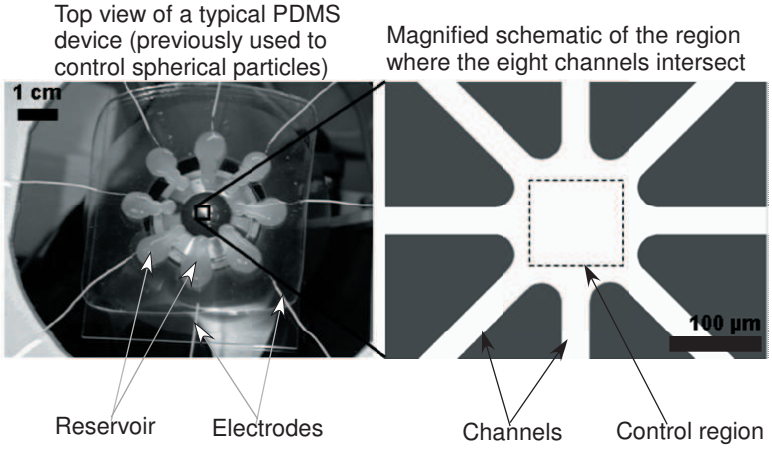

Figure 2. The left panel shows the top view of a typical flow control device. The device is made of PDMS and consists of eight channels that merge into a central region. The electrodes are immersed in reservoirs connected to the channels. The fluid and objects are injected into the reservoirs and then flow into the central region where the channels merge. A magnified schematic of this central region is shown in the right panel. The square region (shown with a dotted black line in the right panel) is the 100 μm × 100 μm control region.

The rest of the paper is organized as follows. Section 2 describes electro-osmotic flow. Section 3 describes the effect of the fluid on the motion of the object. Section 4 discusses the control algorithm that is used to manipulate the flow around the object. We show numerical examples demonstrating object control in Sec. 5 and end with a discussion of additional considerations towards experiments in Secs. 6 and 7.

2. Electro-osmotic flow

At the interface between any solid and an electrolytic fluid, the surface energy of the solid surface is reduced by the adsorption of ions from the fluid onto the oppositely charged ions at the surface of the solid [25, 26]. This results in a charge imbalance in a thin (< 100 nm) fluid layer, termed the diffuse (or Debye) layer adjacent to the wall-fluid interface of the device.

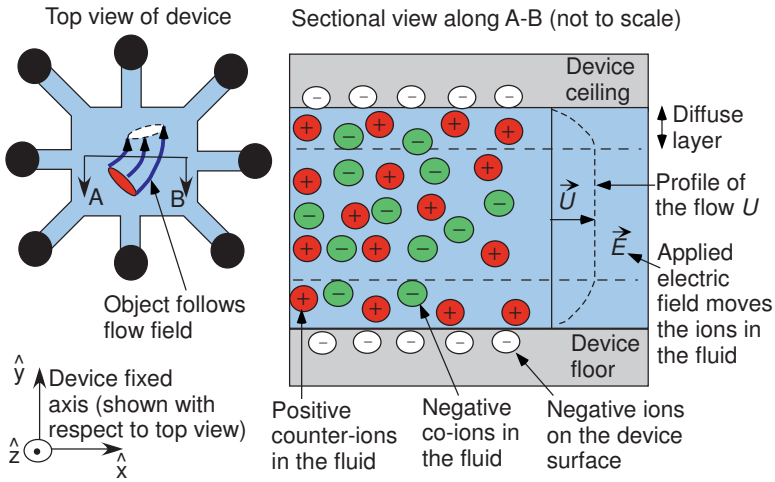

Figure 3. Flow profile in the device (figure in the right panel is modified from [25]): The negatively charged surface of the device is shielded by positively charged ions from the electrolyte solution. The ions in the thin diffuse (Debye) layer near the device-fluid interface move under the influence of the electric field and drag the rest of the fluid by viscous forces [25]. The resulting flow profile is uniform along $\hat{z}$ (except for the variation in the thin diffuse layer, not drawn to scale in the figure) with the flow velocity $\vec{U}$ proportional to the applied electric field $\vec{E}$.

A potential difference applied at the electrodes creates a planar electric field $\vec{E}(\hat{x}, \hat{y})$ in the plane of the device. That electric field moves the ions in the Debye layer which in turn drags the rest of the fluid in the device due to viscosity. The flow is laminar (Reynolds number $< 10^{-4}$), has a steady state velocity profile $\vec{U}(\hat{x}, \hat{y})$ of a plug flow (that is constant along $\hat{z}$ apart from the variation in the thin Debye layer as shown in Fig. 3) which is linearly proportional to the applied electric field, and has the value [25]

$$\vec{U}(\hat{x}, \hat{y}) = \frac{\epsilon\zeta}{\mu} \cdot \vec{E}(\hat{x}, \hat{y}) \tag{1}$$

where μ and ϵ are the dynamic viscosity and permittivity of the fluid respectively, and ζ

is the potential difference across $\hat{z}$ between the edge of the Debye layer and the device-fluid interface.

Since the electric field is irrotational (curl-free) the fluid velocity in the device, which follows the local electric field, is also irrotational. This means EOF can only impart a translational velocity to a spherical object - one cannot rotate a sphere using EOF. However, as described in the next section, EOF can translate as well as rotate a non-spherical object such as an ellipsoid or a nanorod.

3. Translational and rotational velocity of an ellipsoid in electro-osmotic flow

Similar to the inertia-free spherical particles [27] used previously to demonstrate positional control [4, 5], an inertia-free ellipsoid will instantaneously translate along the stream lines of any flow that is set up in the device. If the flow in the device was rotational, one could create a vortex flow and the rotational velocity of a spherical object would be proportional to the vorticity of the flow. However, for an *irrotational* flow, one can nevertheless rotate an ellipsoid due to the interaction of the individual shear components of the flow and the reduced symmetry of the ellipsoid (as compared to a sphere) as shown below. After computing the flow velocity, exact expressions for the force and torque acting on an ellipsoid [30] can be obtained by summing the infinitesimal shear force components (and the resultant torques) acting on every point of the ellipsoid's boundary. For the saddle flow shown in Fig. 4, the net fluidic torque will rotate the ellipsoid clockwise.

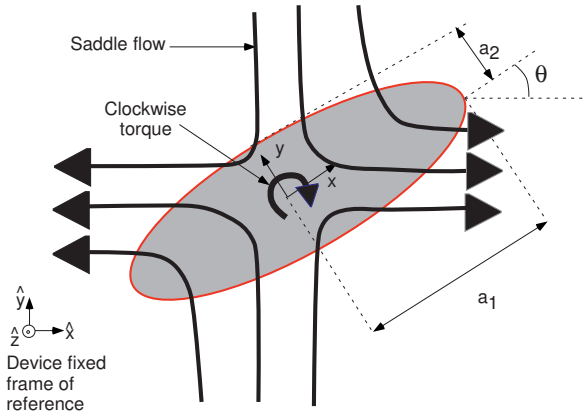

Figure 4. The total torque acting on the body is the sum of infinitesimal torques due to the shear force acting throughout the boundary of the ellipsoid. Due to the unequal axes lengths of the ellipsoid, a saddle flow (illustrated above) can be shown to rotate the ellipsoid clockwise [30]. The body-fixed frame of reference is $x - y$, and the device-fixed frame is $\hat{x} - \hat{y}$.

The slow, viscous, incompressible and isothermal flow that is electro-osmotically set up in the device is well described by Stokes flow [30], which neglects the momentum of the fluid in the Navier-Stokes equations of fluid dynamics. The ellipsoid is controlled

in a plane parallel to the floor of the device and is assumed to lie far enough (> 200 nm) from the floor and ceiling of the device to neglect increased drag due to wall effects [31]. This claim is supported by recent calculations [32] which can be applied, for example, to compute the drag correction terms for a cylindrical particle of diameter 200 nm and length 2 μm, with the nearest point on its surface located at a distance $d = 200$ nm from a plane wall, and its axis tilted at an angle ϕ to the plane of the wall. Detailed simulations [32], performed for such cylinders (with aspect ratios of 10), show that the correction term for the (x, y) translational drag coefficients and the rotational drag coefficient about the z axis are each less than 15% as compared to the unbounded fluid drag coefficients for ϕ as large as 45°. The correction terms decrease as the aspect ratio of the cylinder increases because a proportionately lower area of the rod is close to the wall [32]. Hence, we disregard the wall-correction term and use the unbounded fluid drag coefficients in what follows.

The flow set up in the device is perturbed by the presence of the ellipsoid [33, 34, 35]. The linear nature of Stokes flow can be exploited to obtain the force and torque acting on *any* body (not just an ellipsoid) that is immersed and free to move in the flow. Denote the surface of the ellipsoid by $\frac{x^2}{a_1^2} + \frac{y^2}{a_2^2} + \frac{z^2}{a_3^2} = 1$ (here we consider ellipsoids where $a_3 = a_2$ and $a_1 > a_2$, so a_1 is the semi-major axis length and a_2 is the semi-minor axis length of the ellipsoid). The unperturbed flow field $\vec{u}(\vec{r})$ (i.e., the flow that would be observed if no object were present) in the device is approximated to be a superposition of uniform and pure-shear flow fields, i.e., spatial variations of $\vec{u}(\vec{r})$ of $O(a_1^2)$ or higher are neglected.

Denote the translational velocity of the ellipsoid along the device-fixed axes $\hat{x}, \hat{y}$ (see Fig. 4) as $U_{\hat{x}}$ and $U_{\hat{y}}$ respectively. As shown in Fig. 4, θ is the angle between the body and device fixed frames of reference. Denote the angular velocity of the ellipsoid about the $\hat{z}$ axis as $\omega_{\hat{z}}$. Denote $\hat{u}$ and $\hat{v}$ as the components of the unperturbed uniform flow along the $\hat{x}$ and $\hat{y}$ axes respectively, evaluated at the position that is occupied by the center of the ellipsoid, while the terms $\frac{\partial \hat{u}}{\partial \hat{x}}$, $\frac{\partial \hat{u}}{\partial \hat{y}}$, $\frac{\partial \hat{v}}{\partial \hat{x}}$, and $\frac{\partial \hat{v}}{\partial \hat{y}}$ represent the shear components of the flow. The constant $e = \frac{a_2}{a_1}$ is the ratio of the minor to major axis lengths of the ellipsoid. For the flow $\vec{u}(\vec{r})$ described above, ignoring parasitic pressure flows, and using the assumption of negligible inertia of the ellipsoid, it can be shown [30] that the translational velocity of the ellipsoid matches the uniform flow field component

$$\begin{aligned} U_{\hat{x}} &= \hat{u} \\ U_{\hat{y}} &= \hat{v} \end{aligned} \tag{2}$$

and the rotational velocity of the ellipsoid is given by

$$\begin{aligned} \omega_{\hat{z}} = \frac{1}{2}\Big[\left(\frac{\partial \hat{v}}{\partial \hat{x}} - \frac{\partial \hat{u}}{\partial \hat{y}} \right) + \frac{1-e^2}{1+e^2}\Big(\frac{\partial \hat{u}}{\partial \hat{x}}(-\sin(2\theta)) + \frac{\partial \hat{v}}{\partial \hat{x}}(\cos(2\theta)) \ldots \\ + \frac{\partial \hat{u}}{\partial \hat{y}}(\cos(2\theta)) + \frac{\partial \hat{v}}{\partial \hat{y}}(\sin(2\theta)) \Big) \Big] \end{aligned} \tag{3}$$

Equations 2 and 3 are derived by integrating the shear and pressure distributions on the surface of the inertia-less ellipsoid after solving the quasi-static Stokes equations

[28] (see Section A of the Supplementary Information for more details). Even if higher order spatial flow variations were considered (in addition to uniform and pure shear flow terms), successive correction terms in Eqns. 2 and 3 would differ by the operator $D^2 \equiv a_i^2 \frac{\partial^2}{\partial x_i^2}$ where x_i are the axis coordinates [35]. In the proposed device, these higher order terms are of the order $O(\frac{a_i^2}{r_{dev}^2})$ and higher compared to the linear terms included in Eqns. 2 and 3; where r_{dev} is the distance from the center of the control region to the midpoint of any straight edge at the boundary in Fig. 5. Since $\frac{a_1}{r_{dev}}$ is 0.1 or smaller in the proposed device, we ignore higher spatial order flow variations .

Eqn. 3 can be simplified by making use of two relations between the four shear components. By continuity, the divergence of the flow field is zero, i.e., $\frac{\partial \hat{u}}{\partial \hat{x}} + \frac{\partial \hat{v}}{\partial \hat{y}} = 0$. We also have that in EOF, since the fluid velocity is proportional to the electric field (as explained in the previous section), the flow field is curl-free - i.e., the component of the the vorticity about the $\hat{z}$ axis $(\frac{\partial \hat{v}}{\partial \hat{x}} - \frac{\partial \hat{u}}{\partial \hat{y}})$ (the first term of Eqn. 3), is identically zero. This simplifies Eqn. 3 to

$$\omega_{\hat{z}} = \frac{1-e^2}{1+e^2}\left[\frac{\partial \hat{u}}{\partial \hat{y}}(\cos(2\theta)) + \frac{\partial \hat{v}}{\partial \hat{y}}(\sin(2\theta))\right] \tag{4}$$

Thus, if we apply an electric field that creates the unperturbed flow field $(\hat{u}, \hat{v})$ in the device, then this flow will instantaneously turn the ellipsoid with the rotational velocity $\omega_{\hat{z}}$ in Eqn. 4.

Since the flow velocity components $\hat{u}$ and $\hat{v}$ are linearly dependent on the electric field, the translational and rotational velocity of the object are also linearly dependent on the electric field - a fact that is used in the control algorithm. For any arbitrary orthotropic object (an object with 3 mutually perpendicular planes of symmetry) like the ellipsoidal rod (or other bodies like right elliptical cylinders and rectangular parallelepipeds), the exact same analysis that has been used in this section can be applied to obtain the translational and rotational velocities; the only difference will be a different shape dependent constant, instead of $\frac{1-e^2}{1+e^2}$, in Eqn. 4 [29]. For non-orthotropic objects there will be an additional dependence of the rotational velocity of the object on the fluid velocity (and not just the fluid shear as in Eqn. 4). This is because the force at a particular point on the boundary of the body can give rise to a torque that is not balanced by an opposing torque (due to the lack of sufficient symmetry in the body), thus causing the body to rotate [30]. There will also be an additional dependence of the translational velocity of the object on the fluid shear (and not just the fluid velocity as in Eqn. 2). As explained later, this kind of coupling between the translational and rotational motions of the object can be included by experimenting with an appropriate gain parameter in the control algorithm.

3.1. Translational and rotational Brownian motion of an ellipsoid

Thermal equilibrium between the fluid and any object suspended in it is maintained by the random collisions between the object and the surrounding fluid molecules. The object translates and rotates in a time interval dt along random directions by an amount

that is, on average, proportional to $\sqrt{dt}$. Expressions for the translational and rotational diffusion coefficients [36] of an ellipsoid are given in Section B of the Supplementary information. For the ellipsoids in our simulation (semi-major axis length $a_1 = 5$ μm and semi-minor axis length $a_2 = a_3 = 100$ nm) that are immersed in water of viscosity (8.9×10^{-4}) Pa·s at 300 K, the translational diffusion coefficient along the major axis is 0.306 $\mu m^2/s$ and along the minor axis is 0.199 $\mu m^2/s$. The rotational diffusion coefficient about $\hat{z}$ is 0.0197 rad^2/s. The simulations in Sec.5 account for ellipsoid dynamics due to both fluid flow and Brownian motion.

4. Feedback control of the object's position and orientation

In the presence of Brownian motion of the ellipsoid, one can control the motion of the ellipsoid by using a feedback control algorithm. This control algorithm computes the voltages that need to be applied at the electrodes so that the resultant electric field creates a flow in the device which translates and rotates the object from the currently measured to the desired position and orientation. For any position and orientation of the object, there exists a linear map between the object's velocity and the voltages applied at the electrodes (as explained next). The necessary control electrode voltages can be computed by inverting this map, using least squares. At successive time steps, the object moves to a new position and orientation, there is a new linear map, and we solve another least squares problem to get the next set of electrode voltages. This computation can be done in real time, even for complex situations, as demonstrated in our previous experiments in which we controlled the position of multiple particles at once [5].

The desired trajectory of the ellipsoid is a series of discrete, closely spaced points in the control region with a prescribed desired orientation at each point. At each control update, the difference between the current measured position (orientation) of the object and the desired position (orientation) is multiplied by a proportionality constant called the control gain, yielding the desired (translational and angular) velocity of the object until the next control update. The controller inverts the map between the voltages and the desired translational and rotational velocity to determine the electrode voltages.

We now discuss how to compute this needed linear map which is a composition of three individual maps related to the three physical processes that control the particle motion. In our previous experiments [5], we did not observe any significant spatial or temporal variations in the surface properties of the PDMS or glass substrates, or the viscosity of the fluid, hence we treat the zeta potential, permittivity, and viscosity as spatially and temporally invariant. The first map relates the applied voltages to the resulting electric field (including the gradient of the electric field) in the control region of the device. The second relates the electric field to the fluid flow field in the device. The final map relates the flow field to the object's translational and rotational velocity. We will then show how the composition of these three maps is inverted using least squares.

For the first map, Laplace's equation for the electric potential $\nabla \cdot (\epsilon \nabla(\Phi) = 0$ is evaluated, where ϵ is the permittivity of water and Φ is the electric potential in the domain shown in Fig. 5 (which contains the control region as shown in right panel of Fig. 2).

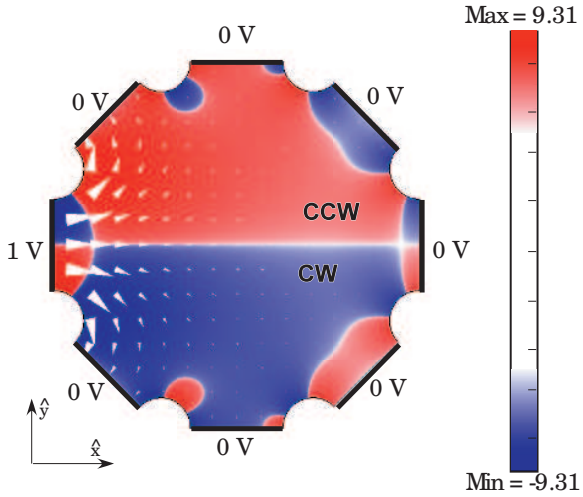

Figure 5. Pre-computed steady state electric field in the region where the channels intersect (using COMSOL, www.comsol.com [37]). The left most edge is maintained at 1 V and all the others are maintained at 0 V. The electric field $E(\hat{x}, \hat{y})$ (which is responsible for the object's translation) is shown with white arrow heads. The color plot shows the ellipse rotation that will be created. For an ellipsoid oriented at $\theta = 0°$, the shear component $\frac{\partial}{\partial \hat{y}}(E_{\hat{x}}(\hat{x}, \hat{y}))$ decides the direction of the ellipsoid's rotation (see Eqn. 4). Thus in the reddish hued region, the ellipsoid will turn counter-clockwise (seeing into the paper) and in the blueish hued region it will turn clockwise. We plot $\text{sign}(\frac{\partial}{\partial \hat{y}}(E_{\hat{x}}(\hat{x}, \hat{y})))\log_{10}(|\frac{\partial}{\partial \hat{y}}(E_{\hat{x}}(\hat{x}, \hat{y}))|)$ to show both the sign and magnitude of the rotation creating term, which varies between $\approx \pm 10^9$ V/m^2.

Eight electric fields are pre-computed, one for each channel. During operation, the electric field (or its gradient) at any point in the control region is a linear superposition of these eight electrical fields. Mathematically, this allows us to write the equations of the first map

$$\begin{pmatrix} E_{\hat{x}}(\hat{x}, \hat{y}) \\ E_{\hat{y}}(\hat{x}, \hat{y}) \\ \frac{\partial}{\partial \hat{y}}(E_{\hat{x}}(\hat{x}, \hat{y})) \\ \frac{\partial}{\partial \hat{y}}(E_{\hat{y}}(\hat{x}, \hat{y})) \end{pmatrix} = [\mathbf{A}(\hat{x}, \hat{y})] \begin{pmatrix} \eta_1 \\ . \\ . \\ \eta_8 \end{pmatrix} \tag{5}$$

where η_i are the applied voltages and the matrix $\mathbf{A}(\hat{x}, \hat{y})$ (of size 4×8) is known for each point $(\hat{x}, \hat{y})$ in the control region using the pre-computed fields.

From Eqn. 1, the fluid velocity at any point in the control region is directly proportional to the electric field. The flow velocity is assumed to reach steady state instantaneously after the potential difference is applied [38] at the electrodes. The fluid shear (spatial gradient of the velocity) is directly proportional to the gradient of the

electric field at that point which gives the second map, between the electric field in the device and the resulting flow and shear field,

$$\begin{aligned}
\hat{u}(\hat{x},\hat{y}) &= \frac{\epsilon\zeta}{\mu}\cdot E_{\hat{x}}(\hat{x},\hat{y}) \\
\hat{v}(\hat{x},\hat{y}) &= \frac{\epsilon\zeta}{\mu}\cdot E_{\hat{y}}(\hat{x},\hat{y}) \\
\frac{\partial}{\partial\hat{y}}(\hat{u}(\hat{x},\hat{y})) &= \frac{\epsilon\zeta}{\mu}\cdot \frac{\partial}{\partial\hat{y}}(E_{\hat{x}}(\hat{x},\hat{y})) \\
\frac{\partial}{\partial\hat{y}}(\hat{v}(\hat{x},\hat{y})) &= \frac{\epsilon\zeta}{\mu}\cdot \frac{\partial}{\partial\hat{y}}(E_{\hat{y}}(\hat{x},\hat{y}))
\end{aligned} \tag{6}$$

If the ellipsoid's center of mass is at the point $(\hat{x},\hat{y})$, then the four relations in Eqn. 6 for the fluid's velocity and the shear at $(\hat{x},\hat{y})$ are the only ones needed for the third map, which relates the fluid's velocity and shear to the object's translational and rotational velocity by Eqns. 2 and 4.

After combining the three maps, the object's translational velocities $U_{\hat{x}}$, $U_{\hat{y}}$, and its rotational velocity $\omega_{\hat{z}}$ are given by the final composite linear map

$$\begin{pmatrix} U_{\hat{x}} \\ U_{\hat{y}} \\ \omega_{\hat{z}} \end{pmatrix} = \frac{\epsilon\zeta}{\mu}\cdot \begin{pmatrix} 1 & 0 & 0 & 0 \\ 0 & 1 & 0 & 0 \\ 0 & 0 & F_c(\theta) & F_s(\theta) \end{pmatrix} [\mathbf{A}(\hat{x},\hat{y})] \begin{pmatrix} \eta_1 \\ . \\ . \\ \eta_8 \end{pmatrix} \tag{7}$$

where η_i are the applied voltages, and $F_c(\theta)$ and $F_s(\theta)$ are given by $F_c(\theta) = \frac{1-e^2}{1+e^2}\cos(2\theta)$ and $F_s(\theta) = \frac{1-e^2}{1+e^2}\sin(2\theta)$. We now show how best to select the 8 electrode voltages to achieve the desired object velocities $U_{\hat{x}}, U_{\hat{y}}, \omega_{\hat{z}}$ that will translate and rotate the object from where it was to where it should be (a similar argument will hold for the general case of N electrodes in an N-channel device).

At every control update we request the desired translational and rotational velocities of the object, which are uncoupled in the case of orthotropic particles like the ellipsoid, to be respectively proportional to the positional and orientational deviations from the desired trajectory. These deviations, or errors, from the desired path are $\varepsilon_{\hat{x}} = \hat{x}_{des} - \hat{x}$, $\varepsilon_{\hat{y}} = \hat{y}_{des} - \hat{y}$ and $\varepsilon_\theta = \theta_{des} - \theta$, so $(\varepsilon_{\hat{x}}, \varepsilon_{\hat{y}})$ is the difference between the desired and current object position and ε_θ is the difference between the desired and current object orientation. The desired object velocities $U_{\hat{x}}$, $U_{\hat{y}}$, and $\omega_{\hat{z}}$ are set to be proportional to the errors $\varepsilon_{\hat{x}}$, $\varepsilon_{\hat{y}}$, and ε_θ by the proportionality gain matrix $\mathbf{K}_{prop}$

$$\begin{pmatrix} U_{\hat{x}} \\ U_{\hat{y}} \\ \omega_{\hat{z}} \end{pmatrix}_{des} = \mathbf{K}_{prop} \begin{pmatrix} \varepsilon_{\hat{x}} \\ \varepsilon_{\hat{y}} \\ \varepsilon_\theta \end{pmatrix} = \begin{pmatrix} K_r & 0 & 0 \\ 0 & K_r & 0 \\ 0 & 0 & K_\theta \end{pmatrix} \begin{pmatrix} \varepsilon_{\hat{x}} \\ \varepsilon_{\hat{y}} \\ \varepsilon_\theta \end{pmatrix} \tag{8}$$

The gains K_r and K_θ are penalties on the translational and orientational errors respectively. A higher value of K_r forces the controller to select voltages that will translate the object to the desired position more quickly. Similarly a higher value of

K_θ forces the controller to select voltages that will rotate the object to the desired orientation quicker. The relative values of K_r and K_θ decide whether the controller spends more of its control authority on the object's translation or on its rotation.

Combining Eqns. 7 and 8 there are more unknowns (the actuator voltages $\vec{\eta} = (\eta_1\, \eta_2\, ..\, \eta_8)^T$) than there are known quantities (the desired velocities $U_{\hat{x}}, U_{\hat{y}}, \omega_{\hat{z}}$). A least square solution, which chooses the minimal size control that achieves the desired velocities, is used to find $\vec{\eta}$. Denote the linear map of Eqn. 7 by the matrix $\mathbf{P}(\hat{x}, \hat{y})$

$$\mathbf{P}(\hat{x}, \hat{y}) = \frac{\epsilon\zeta}{\mu} \cdot \begin{pmatrix} 1 & 0 & 0 & 0 \\ 0 & 1 & 0 & 0 \\ 0 & 0 & F_c(\theta) & F_s(\theta) \end{pmatrix} [\mathbf{A}(\hat{x}, \hat{y})] \tag{9}$$

The least square fit computes the voltages η_i, that minimize the 2-norm [39] of the electrode voltages $||\vec{\eta}||_2$. The optimal voltages are given by

$$\begin{pmatrix} \eta_1 \\ . \\ . \\ \eta_8 \end{pmatrix} = \mathbf{P}^+(\hat{x}, \hat{y}) \mathbf{K}_{prop} \begin{pmatrix} \varepsilon_{\hat{x}} \\ \varepsilon_{\hat{y}} \\ \varepsilon_\theta \end{pmatrix} \tag{10}$$

where $\mathbf{P}^+(\hat{x}, \hat{y}) = (\mathbf{P}^T(\hat{x}, \hat{y})\mathbf{P}(\hat{x}, \hat{y}))^{-1}\mathbf{P}^T(\hat{x}, \hat{y})$ is the pseudo-inverse [39] of the matrix $\mathbf{P}(\hat{x}, \hat{y})$, and $\mathbf{P}^T(\hat{x}, \hat{y})$ is the transpose of the matrix $\mathbf{P}(\hat{x}, \hat{y})$. This is the control law - it states how to compute the electrode voltages given the difference between the actual and desired ellipsoid position and orientation.

As for the control design in our previous experimental work [5], in order to avoid electrolysis (the formation of bubbles at the electrodes that can disrupt the intended flow) we limit the voltages to a maximum value (termed the saturation voltage) $\eta_{sat} = 0.15$ V. Hence the voltages determined in Eqn. 10 are linearly scaled so that this constraint is not violated. If the maximum absolute value of the eight voltages η_i, computed by the controller in Eqn. 10 is η_{max}, then the eight scaled voltages η_i^{scaled} that are eventually applied at the electrodes are given by

$$\eta_i^{scaled} = \left(\frac{\eta_{sat}}{\eta_{max}}\right) \eta_i \quad (1 \leq i \leq 8) \tag{11}$$

Since the ellipsoid velocity is linearly proportional to the applied voltages, this scaling limits the magnitude of the maximum achievable translational and rotational velocity of the object. At every time step this scaling might reduce the magnitude of the object's velocity but not the direction (even after voltage scaling, the particle is steered to correct for the deviation from the desired path, but possibly at a slower speed).

4.1. Non-dimensionalized equations for the feedback loop

A non-dimensionalized version of the governing equations using the flow Peclet numbers is presented here. The relevant physical parameters governing the dynamics are the length scale given by the radius of the control region of the device r_{dev} (in Fig. 5, r_{dev} is the distance from the center of the control region to the midpoint of any straight

edge at the boundary), the saturation voltage η_{sat}, the zeta potential ζ at the fluid-PDMS interface and the fluid's permittivity ϵ, and viscosity μ. In what follows, the non-dimensional parameters are superscripted with an asterisk.

Since the electric field in the device scales as $\frac{\eta_{sat}}{r_{dev}}$, the translational velocity V_{EOF} due to EOF will scale as $V_{EOF} = (\frac{\epsilon\zeta}{\mu})(\frac{\eta_{sat}}{r_{dev}})$. The time needed for the particle to traverse the control region will then scale as $t_{dev} = \frac{r_{dev}}{V_{EOF}}$. The electro-osmotic shear σ_{EOF} generated in the device will scale proportionally to the gradient of the electric field. Since the gradient of the electric field in the control region scales as $\frac{\eta_{sat}}{r_{dev}^2}$, the shear will scale as $\sigma_{EOF} = (\frac{\epsilon\zeta}{\mu})(\frac{\eta_{sat}}{r_{dev}^2})$, so $\sigma_{EOF} = \frac{1}{t_{dev}}$. This scaling of V_{EOF} and σ_{EOF} ignores the contribution of the shape of the control region which is fixed once the number channels and the ratio $\frac{c_{dev}}{r_{dev}}$ are fixed (c_{dev}, the channel width, is the width of the straight edge at the boundary of the control region in Fig. 5). For the rest of this paper, as shown in Fig. 5, the number of channels is fixed at 8, and $\frac{c_{dev}}{r_{dev}}$ at 0.5.

The non-dimensional displacement and time parameters are chosen as $\hat{x}^* = \hat{x}/r_{dev}$, $\hat{y}^* = \hat{y}/r_{dev}$, $\theta^* = \theta$, and $t^* = t/t_{dev}$. The translational $[\hat{u}(\hat{x},\hat{y}),\ \hat{v}(\hat{x},\hat{y})]$ and shear components $[\frac{\partial\hat{u}(\hat{x},\hat{y})}{\partial\hat{y}},\ \frac{\partial\hat{v}(\hat{x},\hat{y})}{\partial\hat{y}}]$ of the flow field and their non-dimensional counterparts $[\hat{u}(\hat{x},\hat{y})^*,\ \hat{v}(\hat{x},\hat{y})^*]$, and $[(\frac{\partial\hat{u}(\hat{x},\hat{y})}{\partial\hat{y}})^*,\ (\frac{\partial\hat{v}(\hat{x},\hat{y})}{\partial\hat{y}})^*]$ are related by $\hat{u}(\hat{x},\hat{y}) = V_{EOF}\cdot\hat{u}(\hat{x},\hat{y})^*$, $\hat{v}(\hat{x},\hat{y}) = V_{EOF}\cdot\hat{v}(\hat{x},\hat{y})^*$, $\frac{\partial\hat{u}(\hat{x},\hat{y})}{\partial\hat{y}} = \sigma_{EOF}\cdot(\frac{\partial\hat{u}(\hat{x},\hat{y})}{\partial\hat{y}})^*$, and $\frac{\partial\hat{v}(\hat{x},\hat{y})}{\partial\hat{y}} = \sigma_{EOF}\cdot(\frac{\partial\hat{v}(\hat{x},\hat{y})}{\partial\hat{y}})^*$. With the non-dimensional map $\mathbf{A}(\hat{x},\hat{y})^*$ chosen as

$$\mathbf{A}(\hat{x},\hat{y})^* = \begin{pmatrix} r_{dev} & 0 & 0 & 0 \\ 0 & r_{dev} & 0 & 0 \\ 0 & 0 & r_{dev}^2 & 0 \\ 0 & 0 & 0 & r_{dev}^2 \end{pmatrix} \mathbf{A}(\hat{x},\hat{y}) \tag{12}$$

the non-dimensional flow components can then be stated in terms of $\mathbf{A}(\hat{x},\hat{y})^*$ as

$$\begin{pmatrix} \hat{u}(\hat{x},\hat{y})^* \\ \hat{v}(\hat{x},\hat{y})^* \\ (\frac{\partial\hat{u}(\hat{x},\hat{y})}{\partial\hat{y}})^* \\ (\frac{\partial\hat{v}(\hat{x},\hat{y})}{\partial\hat{y}})^* \end{pmatrix} = \mathbf{A}(\hat{x},\hat{y})^* \begin{pmatrix} \eta_1^* \\ . \\ . \\ \eta_8^* \end{pmatrix} \tag{13}$$

where the non-dimensional voltages η_i^* are given by $\eta_i^* = \eta_i^{scaled}/\eta_{sat}$ with η_i^{scaled} chosen according to the control law given by Eqn. 10 and 11.

The motion of the ellipsoid is governed by e_1^* $(= \frac{a_1}{r_{dev}})$, e $(= \frac{a_2}{a_1})$, and the rotational Peclet number $Pe_\theta = \sigma_{EOF}/D_\theta$ where D_θ is the rotational diffusion coefficient about $\hat{z}$. Since the expected time for the ellipsoid to rotate by 1 radian about $\hat{z}$ due to diffusion and the applied actuation are $\frac{1}{2D_\theta}$ and $\frac{1}{\sigma_{EOF}}$ respectively, the quantity Pe_θ compares the actuation's ability to compensate for the rotational diffusive motion [40]. A larger value of Pe_θ signifies a higher ability of the actuation to compensate for the diffusive motion about $\hat{z}$. Denoting the translational diffusion coefficients along the major and minor axes of the ellipsoid as D_x and D_y respectively, we define two functions, $T_x^\theta(e) = \frac{D_x}{a_1^2 D_\theta}$ and $T_y^\theta(e) = \frac{D_y}{a_2^2 D_\theta}$, both of which depend solely on the parameter e (see Sec. B.1 of the SI for details). The function $T_x^\theta(e)$ is the ratio of the expected time taken for an

ellipsoid to rotate by 1 radian due to rotational diffusion about $\hat{z}$, to the expected time taken by the ellipsoid to diffuse by a distance a_1 along the major axis of the ellipsoid. Similarly, $T_y^\theta(e)$ is the ratio of the expected rotational diffusion time, to the expected time taken to diffuse by a distance a_2 along the minor axis of the ellipsoid.

With the control law given by Eqns. 8 and 10, the controlled dynamics of an ellipsoid, including the effect of Brownian motion, is as follows. The geometric center translates by an amount $d\hat{x}^*$ along $\hat{x}^*$, $d\hat{y}^*$ along $\hat{y}^*$, while the ellipsoid rotates by an amount $d\theta^*$ about $\hat{z}$ in time dt^* according to the stochastic dynamics update given by

$$\begin{aligned} d\hat{x}^* &= \hat{u}(\hat{x},\hat{y})^* \cdot dt^* + dB_{\hat{x}}^* \\ d\hat{y}^* &= \hat{v}(\hat{x},\hat{y})^* \cdot dt^* + dB_{\hat{y}}^* \\ d\theta^* &= \frac{1-e^2}{1+e^2}\left[\left(\frac{\partial \hat{u}(\hat{x},\hat{y})}{\partial \hat{y}}\right)^* \cos(2\theta^*) + \left(\frac{\partial \hat{v}(\hat{x},\hat{y})}{\partial \hat{y}}\right)^* \sin(2\theta^*)\right] \cdot dt^* + dB_\theta^* \end{aligned} \tag{14}$$

where $dB_{\hat{x}}^*$ and $dB_{\hat{y}}^*$ are the translational Brownian displacements along $\hat{x}$ and $\hat{y}$ respectively and dB_θ^* is the rotational Brownian displacement about $\hat{z}$ which are given by

$$\begin{aligned} dB_{\hat{x}}^* &= \left(\sqrt{\frac{2T_x^\theta(e)dt^*}{Pe_\theta}}e_1^* \cos(\theta^*) - \sqrt{\frac{2T_y^\theta(e)dt^*}{Pe_\theta}}e_2^* \sin(\theta^*)\right) \cdot \mathcal{N}_x(0,1) \\ dB_{\hat{y}}^* &= \left(\sqrt{\frac{2T_x^\theta(e)dt^*}{Pe_\theta}}e_1^* \sin(\theta^*) + \sqrt{\frac{2T_y^\theta(e)dt^*}{Pe_\theta}}e_2^* \cos(\theta^*)\right) \cdot \mathcal{N}_y(0,1) \\ dB_\theta^* &= \left(\sqrt{\frac{2dt^*}{Pe_\theta}}\right) \cdot \mathcal{N}_\theta(0,1) \end{aligned} \tag{15}$$

where $e_2^* = a_2/r_{dev} = e_1^* \cdot e$. The factors $\mathcal{N}_x(0,1)$, $\mathcal{N}_y(0,1)$, and $\mathcal{N}_\theta(0,1)$ denote independent Gaussian random variables with mean 0 and variance 1 which reflect the random character of Brownian motion (see [41] for an introduction to stochastic update formulae). Equations 10-15 describe the controlled motion of the ellipsoid in non-dimensional terms. We simulate this motion for different ellipsoid manipulation tasks and Peclet numbers in the next section.

5. Numerical simulations of an ellipsoid's manipulation

In this section the control law described previously is used to simulate the steering of an ellipsoid along a desired trajectory while the ellipsoid is being perturbed by Brownian motion (according to the controlled ellipsoid dynamics described in Eqns. 10-15). We show how the ellipsoid can be translated and simultaneously rotated as well as rotated in place while trapped at a given location. We will show the dependence of the root mean square (RMS) orientation error (while the ellipsoid is trapped) on Pe_θ and the shape parameter e. We explain the source of this error in detail with a simple Fokker-Planck model which can be used to theoretically predict the trapping error in orientation given the size and aspect ratio of the rod, and the flow parameters.

Parameter	Description	Value
ζ	Zeta Potential at water-PDMS interface	5×10^{-2} V
μ	Viscosity of water	8.9×10^{-4} Pa·s
T	Temperature	300 K
ϵ	Permittivity of water	78.4 ϵ_o[42]
r_{dev}	Radius of control region	100 μm
η_{sat}	Saturation voltage	1.5×10^{-1} V
t_{dev}	Time scale	1.7 s
V_{EOF}	Electro-osmotic velocity	58 μm/s
σ_{EOF}	Electro-osmotic shear	0.58 rad/s
a_1	Major axis length of ellipsoid	5 μm
$a_2 (= a_3)$	Minor axis length of ellipsoid	100 nm

Table 1. Example of parameter values for $e_1^* = .05$, $e = .02$, and $Pe_\theta = 30$.

For showing control over different trajectories, the simulations were performed with parameters $e_1^* = .05$, $e = .02$, and $Pe_\theta = 30$. Table 1 states a sample set of values of the physical parameters that reflect the above non-dimensional numbers.

Unless otherwise stated, the non-dimensional simulation results are stated in degrees for rotation, the translational displacements in units of r_{dev}, time in units of t_{dev}, and applied voltages in units of η_{sat}. The applied voltages are updated every $dt^* = 5.9 \times 10^{-3}$, which corresponds to the 10 ms time lag that is expected in experiments [43]. This time lag occurs due to the finite frame rate of the camera and the computational time required by the control and object vision detection algorithm. The ellipsoid's position and orientation are assumed to be perfectly known in these simulations. The choice of gain coefficients K_r and K_θ (see Eqn. 8) determines the extent to which the control authority is spent on controlling position versus orientation respectively. We experimented with different values of the gain coefficients, for achieving the optimal trade-off between positional and orientational errors in simulations and settled on $\hat{K_r} = K_r * t_{dev} = 1.7 \times 10^6$ and $\hat{K_\theta} = K_\theta * t_{dev} = 8 \times 10^4$ for all the simulations shown here. We will discuss the relation between η_{sat}, the rotational diffusion coefficient, and the gain coefficients at the end of this section. The first simulation is of the ellipsoid tracing a square path, shown in Fig. 6 and 7.

The square path has a side length equal to 0.8. The ellipsoid initially starts off at the bottom left corner of the square and is returned to the same point at the end of the simulation. In the initial part of the simulation (from the bottom left to the top left corner of the square path), the ellipsoid is controlled to move along a straight line, at a constant orientation ($\theta^* = 90°$). Along the next three sides of the square, the ellipsoid is controlled to rotate by 90° by the time it reaches the end of that side (see movie M1 in Supplementary information). The positional and orientation errors are shown in Fig. 8.

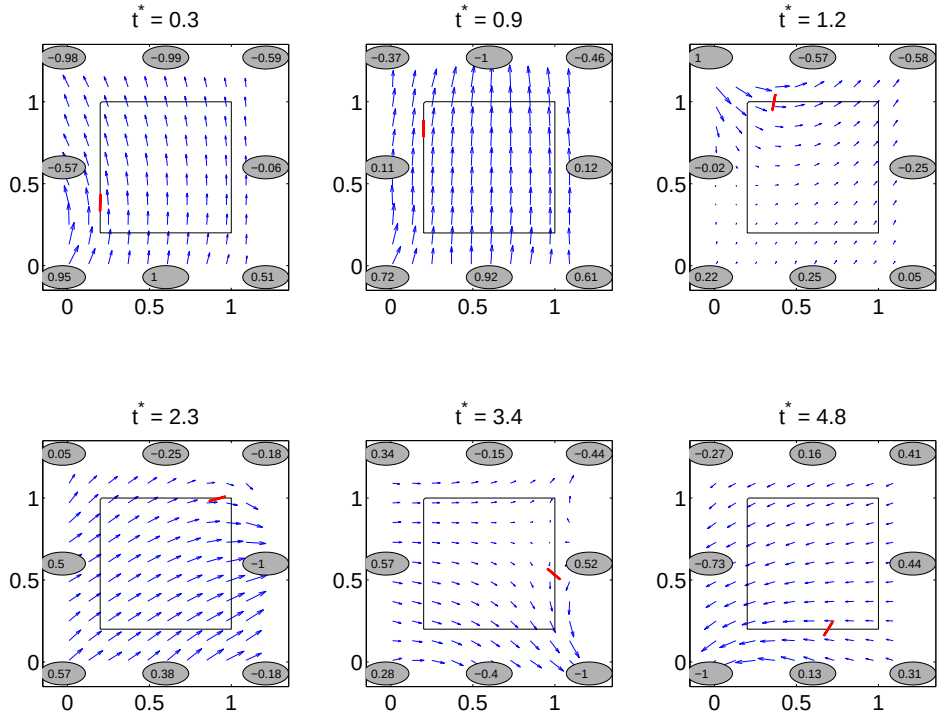

Figure 6. Six snapshots showing the ellipsoid tracing the square path (shown in black). In each snap shot, the flow field is shown with blue arrows and the voltages applied at the eight electrodes are shown inside the gray circles at the periphery. The ellipsoid is continually perturbed by Brownian motion and is controlled and corrected by the flow to start at the bottom left corner of the desired trajectory, trace the square path, and then return to the bottom left corner. While traversing the trajectory from the bottom left corner to the top left corner of the square ($t^* = 0.3$ and $t^* = 0.9$), the ellipsoid is controlled to translate without rotating (an orientation of $\theta = 90°$ is maintained). Then the ellipsoid is controlled to rotate by 90° while translating along each of the remaining three segments of the square. A strobe plot showing only the ellipsoid's position and orientation with respect to the square is shown in Fig. 7.

In Fig.9, we demonstrate the ellipsoid being controlled along a more complex "hour glass" path shape that spans the entire control region. The ellipsoid starts at the bottom left corner of the trajectory at an initial orientation of $\theta^* = 90°$. It is then controlled to move to the top right corner, then to the top left corner, down to the bottom right corner, and finally back to the bottom left corner. While translating, the ellipsoid is controlled to simultaneously rotate so that its major axis is aligned with the each of the four segments of the trajectory by the time it reaches the end of that segment (see movie M2 in Supplementary information).

The next simulation shows the ellipsoid both trapped in place and being rotated from an initial orientation of 90° to a final orientation of 0° by EOF control. The change in orientation of the ellipsoid over time and the associated flow field and electrode

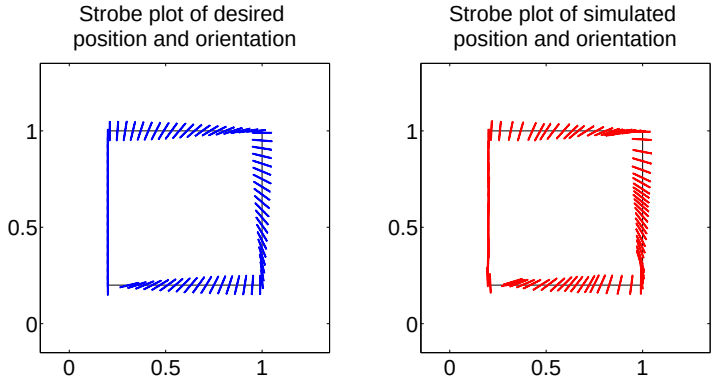

Figure 7. The panel on the left is a strobe plot of the desired orientation of the ellipsoid along different points of the square path. The panel on the right shows a strobe plot of the ellipsoid tracing the square path (shown here for 95 consecutive time steps). The side of the square path (marked in black) measures 0.8 in the non-dimensional length units. The ellipsoid starts in the bottom left corner, traces the path, and returns to the starting point by $t^* = 5.6$.

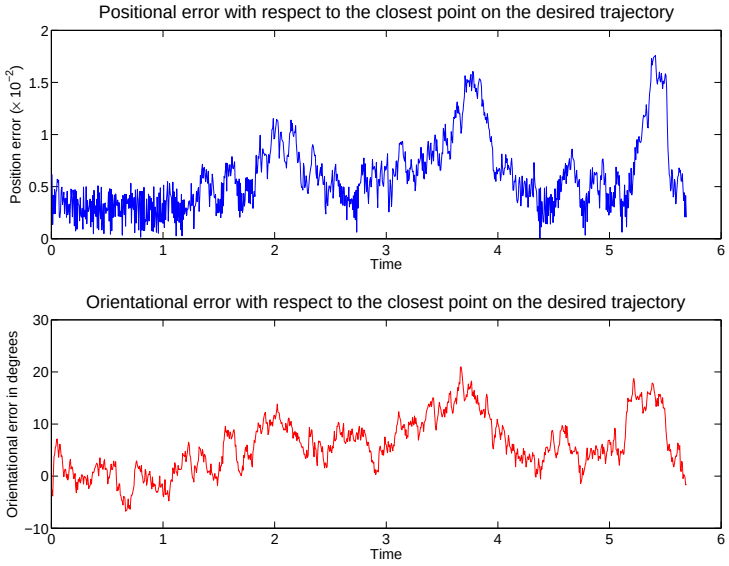

Figure 8. The top and bottom panels show the variation of the positional and orientational errors respectively for the ellipsoid tracing the square path. Denote the coordinates of the ellipsoid at time t_i^* as $(\hat{x}^*(t_i^*), \hat{y}^*(t_i^*), \theta^*(t_i^*))$ and the coordinates that were desired at the previous time step t_{i-1}^* as $(\hat{x}_{des}^*(t_{i-1}^*), \hat{y}_{des}^*(t_{i-1}^*), \theta_{des}^*(t_{i-1}^*))$. The positional error $\varepsilon_{pos}(t_i^*)$ is defined as $\varepsilon_{pos}(t_i^*) \equiv ((\hat{x}^*(t_i^*) - \hat{x}_{des}^*(t_{i-1}^*))^2 + (\hat{y}^*(t_i^*) - \hat{y}_{des}^*(t_{i-1}^*))^2)^{\frac{1}{2}}$. The orientational error $\varepsilon_{\theta^*}(t_i^*)$ is defined as $\varepsilon_{\theta^*}(t_i^*) \equiv \theta^*(t_i^*) - \theta_{des}^*(t_{i-1}^*)$. For the first side of the square ($0 < t^* < 1.2$), apart from countering rotational Brownian motion, there was no need to rotate the ellipsoid. Hence the available control authority could be committed more fully to correcting positional errors. At subsequent stages, the need to turn the ellipsoid leads to a decreased capability to correct positional errors.

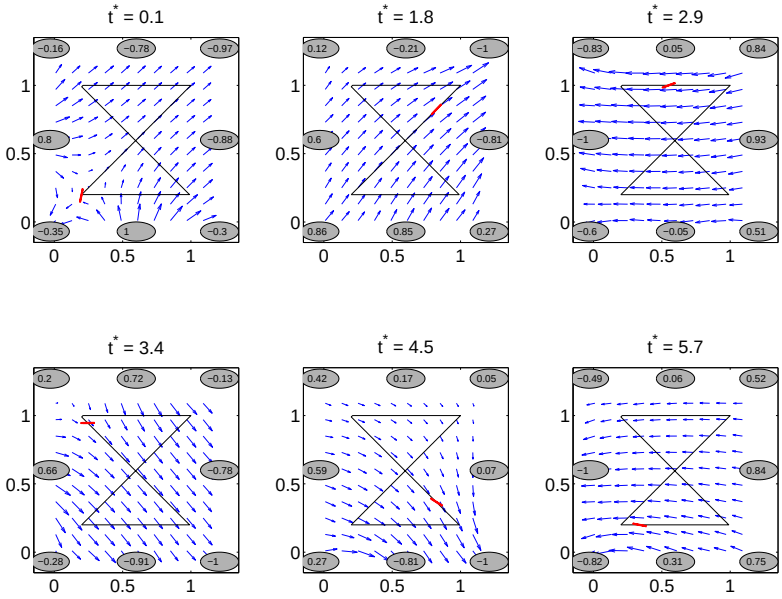

Figure 9. Six snapshots showing the ellipsoid tracing the "hour glass" path (shown in black) that spans the majority of the control region. The ellipsoid starts at the bottom left corner of the desired trajectory, traces the path, and then is returned to the bottom left corner. Along each of the 4 segments of the desired trajectory, the orientation task is to align the major axis of the ellipsoid along that segment by the time it reaches the end of that segment.

voltages are shown in Fig. 10 (see movie M3 in Supplementary information).

In the initial part of the simulation (until $t^* = 1.17$), the controller spends most of its control authority on rotating the ellipsoid from $\theta = 90°$ to $\theta = 0°$ compared to correcting for positional error due to translational Brownian motion. This results in a non-zero mean translational error of 1.9×10^{-4} in position, with root mean square (RMS) of 1.3×10^{-4}. In the tail end of the above simulation, when the ellipsoid is nominally trapped at the desired location and orientation, as shown in Fig. 12, we observe an RMS error in the orientation angle. The RMS error in orientation, RMS_{sim}, is computed from the simulations in the following manner

$$RMS_{sim} = (\frac{1}{n} \sum_{i=m}^{i=m+n} (\theta^*(t_i^*) - \overline{\theta^*})^2)^{\frac{1}{2}} \tag{16}$$

where $\theta^*(t_i^*)$ is the orientation of the ellipsoid at the i^{th} time step. There are a total of $(m+n)$ time steps in the simulation, the ellipsoid first reaches $\theta^* = 0°$ at the m^{th} time step (termed the first passage time), then $\overline{\theta^*} = \frac{1}{n+1}(\sum_{i=m}^{i=m+n} \theta(t_i^*))$. This RMS error is a result of the competition between Brownian motion and the controller. The rotational Brownian motion of the ellipsoid will tend to rotate the ellipsoid away from $\theta^* = 0°$, while the controller tries to bring it back to $\theta^* = 0°$.

Since the rotational dynamics depends on the rotational Peclet number Pe_θ and

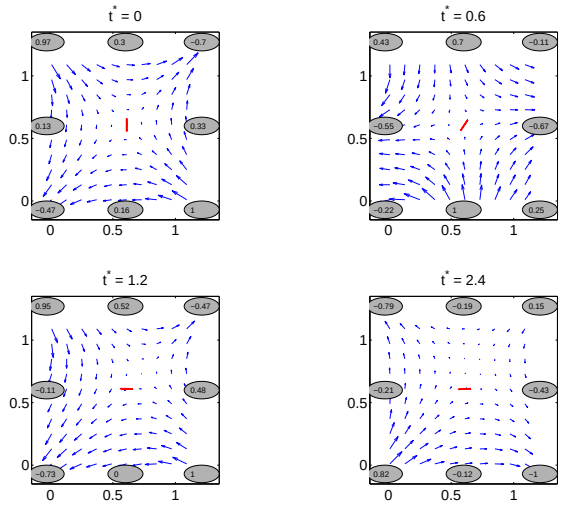

Figure 10. Four snapshots showing the ellipsoid rotating by 90°. In each snap shot, the flow field is shown with blue arrows and the voltages applied at the eight electrodes are shown inside the gray circles at the periphery. The ellipsoid has been rotated by 90° by $t^* = 1.2$ after which the controller continuously adjusts voltages to counteract Brownian motion and maintain the ellipsoid in place at $\theta^* = 0°$.

the shape parameter e, we plot the dependence of the RMS trapping error as a function of these variables in Fig. 11. For better visualization, the error is plotted against the aspect ratio $1/e$. As one would expect, the orientation error decreases with increasing Pe_θ because of comparatively larger actuation compensating for the particle's diffusive motion. For a fixed Pe_θ, the plot shows a sharp increase in error as the aspect ratio approaches 1, i.e., as the shape of the ellipsoid approaches that of the sphere (unit aspect ratio). In addition there is a slow increase in error, for a fixed Pe_θ, as the aspect ratio increases (compare errors between aspect ratios 10 and 50). We explain this next.

5.1. Fokker Planck equation describing the orientation error

It is possible to theoretically estimate the variation of the RMS error in orientation, termed RMS_{theor}, with respect to the size and the aspect ratio of the ellipsoid as

$$\begin{aligned} RMS_{theor} &= \sqrt{2}\left(\frac{1+e^2}{1-e^2}\right)\left(\frac{D_\theta}{\sigma_{max}}\right) \\ &\equiv \sqrt{2}\left(\frac{1+e^2}{1-e^2}\right)\left(\frac{kT}{\mu}\right)\left(\frac{g(e)}{a_1^3}\right)\left(\frac{1}{\sigma_{max}}\right) \end{aligned} \tag{17}$$

where RMS_{theor} is in radians, σ_{max} is the maximum rotational velocity with which one can turn the ellipsoid and $D_\theta \equiv \left(\frac{kT}{\mu}\right)\frac{g(e)}{a_1^3}$ (see [36] and expressions for the rotational diffusion coefficient in Section B of the Supplementary Information to see that D_θ is inversely proportional to a_1^3). The value of σ_{max} equals the maximum allowable fluid shear that can be actuated by the electrodes under the constraint that the applied

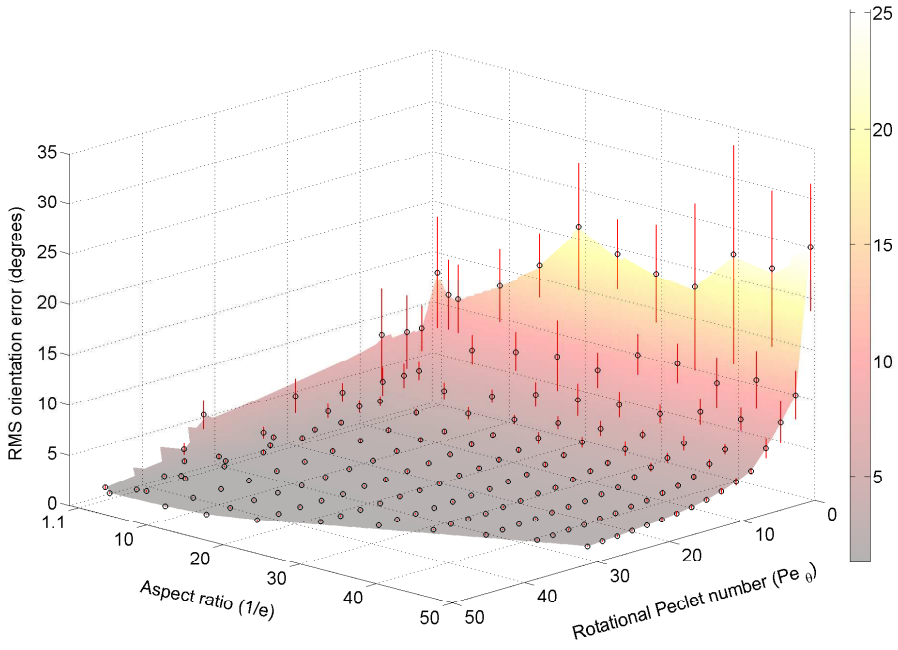

Figure 11. Effect of aspect ratio and rotational Peclet number on RMS orientation error: The parameter e_1^*, which corresponds to the semi-major axis length of the ellipsoid, was fixed at the value 0.05. For each (Pe_θ, e), the plotted values are the average of 10 runs of the simulation with the ellipsoid being nominally trapped at 0°. The error bar for each average is plotted on the graph, while a surface is fitted to the data to guide the eye. Increasing values of Pe_θ means that more shear is available to compensate the perturbation due to the rotational Brownian motion of the ellipsoid, thus decreasing the error. For a fixed Pe_θ, there is a sharp increase in error as the shape of the ellipsoid approaches that of the sphere (aspect ratio ≈ 1.1). This effect is explained in the text.

voltages do not exceed η_{sat}. In terms of Pe_θ, Eqn. 17 can be rewritten as

$$RMS_{theor} = \sqrt{2}\left(\frac{1+e^2}{1-e^2}\right)\left(\frac{1}{\sigma^*_{max} Pe_\theta}\right) \tag{18}$$

where σ^*_{max} is the non-dimensional maximum shear that only depends on the shape of the device, i.e., on the number of channels and the device geometry parameter $\frac{c_{dev}}{r_{dev}}$.

A derivation of the expression in Eqn. 17 makes use of two observations noted in the simulations. First, the controller spends most of its control authority in maintaining the ellipsoid's orientation at $\theta = 0°$ and relatively less authority on position control. Second, as seen in the bottom panel of Fig. 12 (which corresponds to $e_1^* = .05$, $e = .02$, and $Pe_\theta = 30$), the controller exerts this authority by maintaining the value of the shear component $\left(\frac{\partial \hat{u}}{\partial \hat{y}}\right)^*$ at the maximum of ± 1.6 for most time steps after $t^* \approx 1.1$ (when it is first oriented at $\theta^* = 0°$). It abruptly switches between ± 1.6 as needed in order to counter the rotational Brownian motion of the ellipsoid. Thus the controller essentially executes a simple *bang-bang*-type control law [44] for maintaining the ellipsoid's orientation at $\theta^* = 0°$: it checks whether the ellipsoid has

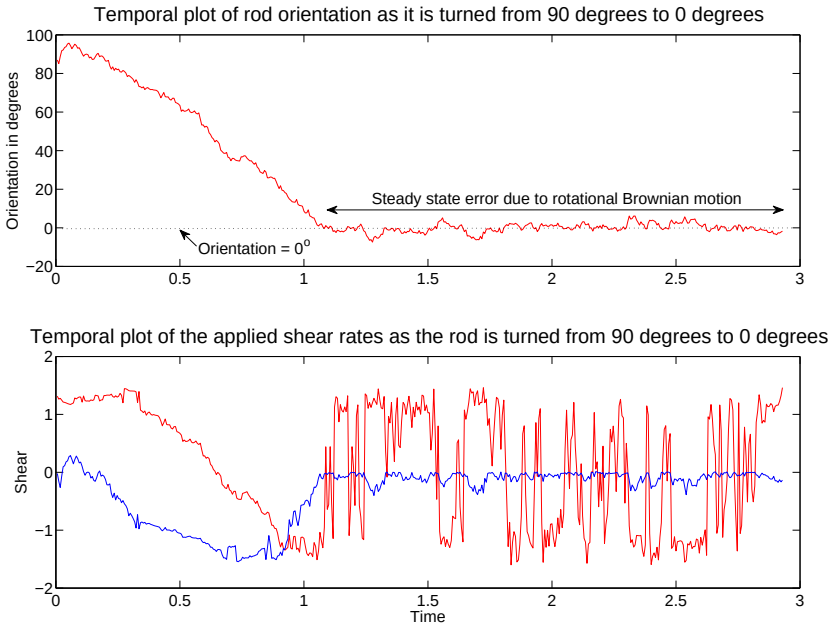

Figure 12. The top panel shows the temporal trace of the ellipsoid's orientation as it is being turned by 90°. The bottom panel shows the temporal trace of the 'unperturbed' fluid shear rates, $(\frac{\partial \hat{u}}{\partial \hat{y}})^*$ in red and $(\frac{\partial \hat{v}}{\partial \hat{y}})^*$ in blue, computed at the geometric center of the ellipsoid. For most of the time steps after $t^* = 1.2$, the controller can be seen to maintain the value of the shear component $(\frac{\partial \hat{u}}{\partial \hat{y}})^*$ at the maximum it can create, ± 1.62, or it abruptly switches between these values. This switching counters the rotational Brownian motion of the ellipsoid and maintains its orientation at $\theta^* = 0°$.

positive orientation $\theta^* > 0°$, or negative orientation, $\theta^* < 0°$, and attempts to apply the maximum allowable shear ($\sigma^*_{max} = 1.6$), that can rotate the ellipsoid back to $\theta^* = 0°$. The associated Fokker-Planck equation for the probability distribution function of θ that arises from the stochastic differential equation that describes the above simplified control law yields Eqn. 17, as explained in detail in Section C of the Supplementary Information.

In Fig. 13 we compare RMS_{theor}*and* and RMS_{sim} for a range of ellipsoid sizes a_1 and aspect ratios $\frac{a_1}{a_2}$ (note: $e = \frac{a_2}{a_1}$). The simulations for computing RMS_{sim} were performed with the flow parameters stated in Table 1, with the ellipsoid being trapped by EOF control at the center of the control region. For plotting RMS_{theor} we set the maximum shear, which is a property of the device/controller and not the ellipsoid, as $\sigma_{max} = 0.94$ rad/s (corresponding to $\sigma^*_{max} = 1.6$ shown in Fig. 12). Given that we disregard any loss of control authority for position control in the simple model of the control law that was used to derive RMS_{theor}, the good match between RMS_{sim} and RMS_{theor} for the range of particle sizes and aspect ratios under consideration verifies that most of the controller's authority is indeed spent in controlling the orientation rather than the position of the ellipsoid.

For a fixed aspect ratio, the rotational diffusion coefficient varies inversely as a_1^3

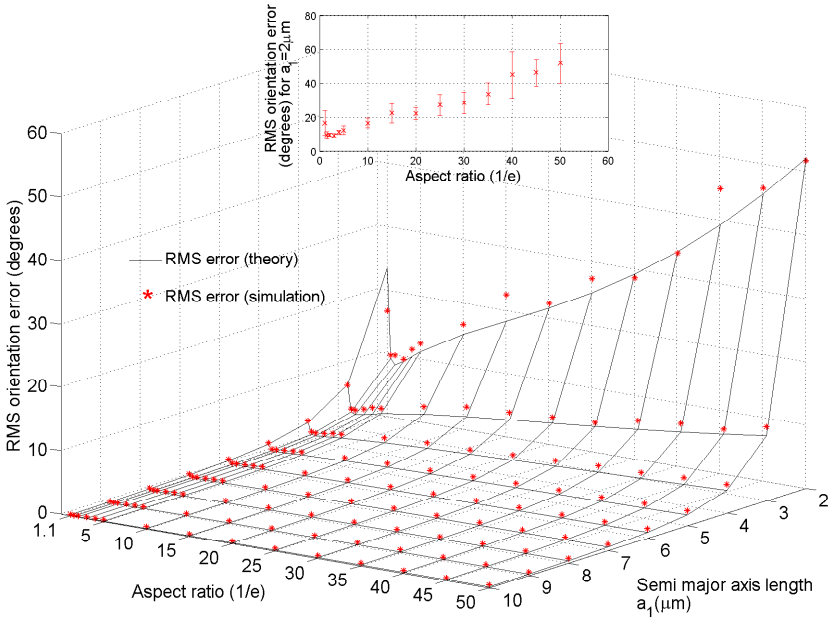

Figure 13. Comparison of RMS errors in orientation between the theoretical estimate RMS_{theor} (Eqn. 17) and the simulation based estimate RMS_{sim} (Eqn. 16) for flow parameters stated in Table 1. For each ellipsoid size and aspect ratio, the plotted value of RMS_{sim} is the average of 10 runs of the simulation with each run lasting 50 seconds while the ellipsoid was trapped at the center of the control region. The error bars for the simulation based estimate RMS_{sim} are shown in the inset for $a_1 = 2$ μm, while the error bars for other values of a_1 are too small to depict on the plot. The plot shows the increase in RMS error due to the increase in the diffusion coefficient as the ellipsoid size (a_1) decreases. For a fixed a_1, the plot shows an increase in RMS error at the highest and lowest values of the aspect ratios ($\frac{a_1}{a_2}$) with a dip in RMS error at $\frac{a_1}{a_2} \approx 2$. The diffusion coefficient increases weakly with aspect ratio. Consequently, for a fixed size a_1, there is a comparatively slow increase in RMS error seen for values $\frac{a_1}{a_2} > 5$ in the plot. As the aspect ratio decreases ($\frac{a_1}{a_2} \to 1$), there is a sharper increase in RMS error due to the term $\frac{1+e^2}{1-e^2}$ in Eqn. 17. This effect is noticeable for smaller ellipsoids ($a_1 \leq 3$ μm). The good match between RMS_{theor} and RMS_{sim} shows that orientation control is harder to achieve and so the controller spends most of its authority in controlling orientation rather than position. The ellipsoid size $a_1 = 3$ μm and the aspect ratio $\frac{a_1}{a_2} = 1.2$ are seen to be lower bounds for maintaining an RMS error of 5°.

(as opposed to the translational diffusion coefficient which is inversely proportional to a_1). Hence as a_1 decreases, the RMS error should increase as seen in Fig. 13. The increase in aspect ratio ($\frac{a_1}{a_2}$), for fixed a_1, causes a comparatively weaker increase in the diffusion coefficient, and consequently in the RMS error. For a fixed a_1, the aspect ratio dependent term $\frac{1+e^2}{1-e^2}$ (in Eqn. 17) increases the RMS error as $e \to 1$. This is observed in Fig. 13, more noticeably for smaller particles, at $\frac{a_1}{a_2} = 1.1$. This increase in RMS error reflects the loss in the ability of a curl-free flow to rotate a near-spherical shaped particle.

In other work by our group [6], we have been able to experimentally show position control of nanoscopic particles by EOF based position control in a highly viscous fluid. This was possible because the actuation was not saturated while trying to control the particle position but the increased viscosity reduced the translation diffusion coefficient. However this avenue is not feasible for orientation control because the actuation does saturate while trying to compensate for rotational diffusion. Thus the effectiveness of rotational control is set by actuator saturation. The rotational Peclet number Pe_θ is independent of fluid viscosity. Seen in dimensional terms, the rotational diffusion coefficient D_θ as well as the maximum shear σ_{max} (which was set as the maximum value of the fluid shear $\frac{\partial}{\partial \hat{y}}(\hat{u})$ observed in Fig. 12) are both inversely proportional to the fluid viscosity (see Eqn. 11 in Section B of the Supplementary information for an expression of the diffusion coefficient and Eqn. 6 in the main text for the shear field). Hence increasing the fluid viscosity does not decrease the value of the RMS error in orientation (since $RMS_{theor} \approx \frac{D_\theta}{\sigma_{max}}$). Thus, in the control model described in this paper, for the flow parameters stated in Table 1, even though slender particles (where $a_2 = 100$ nm for example) can be controlled, $a_1 = 3$ μm and $\frac{a_1}{a_2} = 1.2$ are seen to be lower bounds on the particle size and aspect ratio for maintaining RMS errors in orientation of around 5°, irrespective of the fluid viscosity. Since the control voltages are not allowed to exceed η_{sat}, penalizing the orientation error in Eqn. 10 by indefinitely increasing the control gain K_θ does not reduce the orientation error below what is allowable by the maximum shear σ_{max}. Instead one could reduce electrolysis at the electrodes by protecting them with a film of nafion [45]. This would allow for an increased value of η_{sat}, and hence an increased value of σ_{max}, thus reducing the RMS error. This will be investigated in future experiments.

6. Additional considerations towards experiments

In this section we consider additional features that will be important for future experiments and applications. We first consider the effect of the size and shape of more general objects for flow control. For other types of orthotropic particles, for example a cylinder, there will be a different constant, instead of $\frac{1-e^2}{1+e^2}$, that determines the rotational velocity of the particle in Eqn. 4. This constant can be computed by simulating the flow around the cylinder with the Stokes flow equations (described in Section A of the Supplementary Information) and integrating the resulting shear and pressure distributions on the surface of the cylinder. The cylinder's motion can be controlled using a similar control law modified with this new constant. Also in experiments, the exact size of the cylinder can only be known to a certain precision. Since the control voltages depends on the object size (through the $\mathbf{P}(\hat{x}, \hat{y})$ matrix in Eqn. 9) as well as on the gain matrix $\mathbf{K}_{prop}$ in Eqn. 10, one could compensate for the imprecise knowledge of the object size by experimenting with the value of $\mathbf{K}_{prop}$ until a suitable performance is achieved.

For non-orthotropic particles, since translation and rotation are coupled, the

structure of the $\mathbf{P}(\hat{x}, \hat{y})$ matrix will change. In particular, some of the elements of the matrix that premultiplies $\mathbf{A}(\hat{x}, \hat{y})$ in Eqn. 9 will have a non zero value. However one can still compute the pseudo-inverse of $\mathbf{P}(\hat{x}, \hat{y})$ and obtain the control voltages, after one makes an appropriate choice of $\mathbf{K}_{prop}$. In this case $\mathbf{K}_{prop}$ should be chosen to be non-diagonal to ensure that orientation and position errors are penalized in a manner that accounts for the coupling between translation and rotation.

We have shown simulations in which the object is being controlled in two dimensions, however the translational diffusion of the object in the z direction and the rotational 'pitching' diffusion about the body-fixed y axis can bring the object in contact with (and thus might make it stick to) the glass and PDMS surfaces that form the floor and ceiling of the device respectively. However, the object may have a natural electrostatic repulsion to the wall and if not, coatings can be applied to the device that will prevent sticking of the object to the device [46]. With such coatings and by considering devices that are thin with respect to the object length one can mitigate the tendency of the object to pitch out of the plane in which it is being controlled. Even when the object pitches out of plane, one does not completely lose the ability to control the rod in the plane of the device. As long as the pitching angle is small, one should expect to control the rotation about $\hat{z}$ (normal to the device plane) with the same control law as proposed in this paper, with a modified rotational gain K_θ (see Eqn. 8).

Our control algorithm assumes that the object velocity exhibits a linear dependence on the electric field (see Eqns. 2 and 4). However, the object itself might have a charged Debye layer at its interface with the surrounding fluid. In the presence of an applied electric field, the ions in the Debye layer will move the local fluid surrounding the object, which can in turn impart an unintended translational and rotational velocity to the object. Such an electrophoretic motion of the particle, due to its own (uniform) zeta potential, is linearly dependent on the electric field [47] and can be readily accommodated within our control law as explained in Section D of the supplementary information.

However, depending on whether the object is strongly polarizable, one could observe a quadratic dependence of the velocity on the electric field, as opposed to the strictly linear dependence described in the previous section. This quadratic dependence is induced charge electrophoresis (ICEP) [48, 49, 50, 51]. This effect is explained in Section D of the supplementary information where we show that the magnitude of the rotational velocity of the ellipsoid due to ICEP using the approximations used by Saintillan et al. [51] is negligible (less than 6 % of that due to EOF) due to the low electric field strengths (less than 7 V/cm) at the ellipsoid's location in the control region. The translational velocity of the ellipsoid due to ICEP is identically zero [51]. This matches well with experimental results [52], where the rotational velocity of a comparably sized object (6 μm $\times$ 300 nm) in water due to ICEP was noticeable only at electric field strengths that were greater than 30 V/cm. Hence this nonlinear effect can be safely neglected in our simulations.

7. Conclusion

We have described the physics that shows how a planar electro-osmotic flow translates and rotates an object that is immersed in it. The map describing this physics can be inverted to obtain a control law that allows one to manipulate the position and orientation of the object by electrically actuating the flow. Our simulations and theoretical model show how the performance of the algorithm scales with the size and aspect ratio of an ellipsoidal object and we have explained how this approach can be extended to objects of more general shapes. In order to realize what we have discussed experimentally, we need to extend our vision algorithm to also estimate the orientation of objects. The vision algorithm has to be robust to the uncertainty in measurement due to pixelation in the camera sensor, dark noise from the camera, low photon counts if the objects are dimly fluorescent, or measurement noise due to imperfect estimation of a small metallic object's orientation from its scattered light. We are currently developing the needed vision algorithms as well as implementing our control methods in hardware, to demonstrate position and orientation control of one and multiple objects simultaneously in experiments. These results will be reported in future publications.

Acknowledgements

The authors would like to thank Peter Carmichael, Gregg Gallatin and Jabez McClelland, all affiliated with the Center for Nanoscale Science and Technology (CNST) at National Institute of Standards and Technology (NIST), Gaithersburg, MD, USA and Matthew McMahon at Naval Surface Warfare Center, West Bethesda, MD, USA (formerly at CNST), for stimulating discussions. The authors are grateful to Klint Rose at Lawrence Livermore National Labs, Livermore, CA, USA and Juan Santiago at Stanford University, Stanford, CA, USA for helpful discussions on induced charge electro-osmosis. We also acknowledge helpful discussions with Joseph Hubbard at NIST, Gaithersburg, MD, USA on fluid dynamics of nano-objects. The first author was supported by the CNST-UMD cooperative grant.

Supporting Information, including movies are available

References

[1] D.J. Sirbuly, M. Law, H. Yan, and P. Yang,"Semiconductor Nanowires for Subwavelength Photonics Integration," *Journal of Physical Chemistry B*, 109, pp.15190-15213, 2005.

[2] B. Messer, J. H. Song, and P. Yang, "Microchannel Networks for Nanowire Patterning," *Journal of the American Chemical Society*, 122, pp.10232-10233, 2000.

[3] A. Minerick, R. Zhou, P. Takhistov, H. Chang, "Manipulation and Characterization of Red Blood Cells with Alternating Current Fields in Microdevices," *Electrophoresis*, 24, pp.3703-3717, 2003.

[4] S. Chaudhary and B. Shapiro, "Arbitrary Steering of Multiple Particles Independently in an Electro-osmotically driven microfluidic system," *IEEE Transactions on Control Systems Technology*, 14, 4, pp.669-680, July 2006.

[5] M. D. Armani, S. V. Chaudhary, R. Probst, and B. Shapiro, "Using feedback control of microflows to independently steer multiple particles," *Journal of Microelectromechanical Systems*, 15, 4, pp. 945-954, August 2006.

[6] C. Ropp, R. Probst, Z. Cummins, R. Kumar, A. Berglund, S. R. Raghavan, E. Waks, and B. Shapiro, "Manipulating Quantum Dots to Nanometer Precision by Control of Flow," *Nano Letters*, 10, 7, pp. 2525-2530, May 2010.

[7] M. E. J. Friese, T. A. Nieminen, N. R. Heckenberg, and H. Rubinsztein-Dunlop, "Optical alignment and spinning of laser-trapped microscopic particles," *Nature*, 394, pp.348-350, July 1998.

[8] A. La Porta and M. D. Wang, "Optical TorqueWrench: Angular Trapping, Rotation, and Torque Detection of Quartz Microparticles," *Physical Review Letters*, 92, 190801, May 2004.

[9] V. Bingelyte, J. Leach, J. Courtial, and M. J. Padgetta"Optically controlled three-dimensional rotation of microscopic objects," *Applied Physics Letters*, 82, 5, pp.829-831, February 2003.

[10] A. T. ONeil and M. J. Padgett, "Rotational control within optical tweezers by use of a rotating aperture," *Optics Letters*, 27, 9, pp.743-745, May 2002.

[11] R. Dasgupta, P.K. Mohanty, and P.K. Gupta, "Controlled Rotation of biological microscopic objects using optical line tweezers," *Biotechnology Letters* , 25, pp.1625-1628, 2003.

[12] L. Paterson, M. P. MacDonald, J. Arlt, W. Sibbett, P. E. Bryant, K. Dholakia, "Controlled Rotation of Optically Trapped Microscopic Particles," *Science*, 292, pp.912-914, May 2001.

[13] K. C. Neuman, E. H. Chadd, G. F. Liou, K. Bergman, and S. M. Block, Characterization of Photodamage to Escherichia coli in Optical Traps, Biophysical Journal, 77, 5, pp. 2856-2863, 1999.

[14] L Zhang, J. J. Abbott, L. Dong, B. E. Kratochvil, D. Bell, and B. J. Nelson,"Artificial bacterial flagella: Fabrication and magnetic control," *Applied Physics Letters* 94, 064107 February 2009.

[15] L. Sacconi, G. Romano, R. Ballerini, M. Capitanio, M. De Pas, and M. Giuntini, "Three-dimensional magneto-optic trap for micro-object manipulation," *Optics Letters*, 26, 17, pp.1359-1362, September 2001.

[16] L. Zhang, J. J. Abbott, L. Dong, K. E. Peyer, B. E. Kratochvil, H. Zhang, C. Bergeles, and B. J. Nelson, "Characterizing the Swimming Properties of Artificial Bacterial Flagella," *Nano Letters*, 9, 10, pp. 3663-3667, September 2009.

[17] D.H. Reich, M. Tanase, A. Hultgren, L.A. Bauer, C.S. Chen, G.J. Meyer, "Biological Applications of multifunctional magnetic nanowires," *Journal of Applied Physics*, 93, 10, pp. 7275-7280, May 2003.

[18] B. Edwards, N. Engheta, and S. Evoy,"Electric tweezers: Experimental study of positive dielectrophoresis-based positioning and orientation of a nanorod," *Journal of Applied Physics*, 102, 024913, July 2007.

[19] S. Raychaudhuri, S. A. Dayeh, D. Wang, and E. T. Yu,"Precise Semiconductor Nanowire Placement Through Dielectrophoresis," *Nano Letters* , 9, 6, pp. 2260-2266, May 2009.

[20] K.D. Hermanson, S.O. Lumsdon, J.P. Williams, E.W. Kaler, and O.D. Velev, "Dielectrophoretically assisted assembly of electrically functional microwires from nanoparticle suspensions," *Science*, 294, pp.1082-1086, November 2001.

[21] P.A. Smith, C.D. Nordquist, T.N. Jackson, and T.S. Mayer, "Electric-field assisted assembly and alignment of metallic nanowires," *Applied Physics Letters*, 77, 9, pp.1399-1401, August 2000.

[22] A. Jamshidi, P. J. Pauzauskie, P. J. Schuck, A. T. Ohta, P. Chiou, J. Chou, P. Yang, and M. C. Wu"Dynamic manipulation and separation of individual semiconducting and metallic nanowires," *Nature Photonics*, 2, pp. 85-89, February 2008.

[23] W. Ahmed, E. S. Kooij, A. van Silfhout, and B. Poelsema, "Quantitative Analysis of Gold Nanorod Alignment after Electric Field-Assisted Deposition," *Nano Letters*, 9, 11, pp. 37863794, 2009.

[24] L. Altomare, M. Borgatti, G. Medoro, N. Manaresi, M. Tartagni, R. Guerrieri, and R. Gambari, "Levitation and Movement of Human Tumor Cells Using a Printed Circuit Board Device based on Software-controlled Dielectrophoresis," *Biotechnology and Bioengineering* , 82, 4, pp.474-479, May 2003.

[25] R.F. Probstein, *Physicochemical Hydrodynamics*, New York, Wiley, 1994.

[26] J. Lyklema, *Fundamentals of Interface and Colloid Science - Volume II Solid-liquid Interfaces* San Diego, Academic Press Inc., 1991.

[27] A simple calculation using Newton's laws [4], shows that a spherical particle of diameter 10 micrometers with a density equal to that of water, takes 0.04 ms to reach the ambient translational flow velocity. This interval is small compared to the expected 10 ms between successive control updates which allows us to assume that the nanorods (major axis length of 10 μm and minor axes length of 200 nm) have negligible inertia and their velocity instantaneously conforms to the local flow field. If the moment of inertia of the sphere is denoted as I_s and the rotational drag coefficient as Ω_s, then a similar calculation for rotation shows that a time $t_r = \frac{I_s \cdot log(\beta)}{\Omega_s} = \frac{\rho a^2 log(\beta)}{15\mu}$ is needed for the sphere to reach within $\frac{1}{\beta}$ of the ambient rotational flow velocity of the fluid (ρ and μ are the density and viscosity of the fluid respectively and a is the sphere radius). For the above sphere in water, $t_r \approx .01$ ms for $\beta = 1000$.

[28] G.B. Jeffery, "The motion of ellipsoidal particles immersed in a viscous fluid," *Proceedings of the Royal Society of London, Series A*, 102, pp.161-179, 1922.

[29] F.P. Bretherton, "The motion of rigid particles in a shear flow at a low Reynolds number," *Journal of Fluid Mechanics*, 14, pp.284-304, 1962.

[30] H. Brenner, "The Stokes resistance of an arbitrary particle - Part IV. Arbitrary fields of flow" *Chemical Engineering Science*, 19, pp. 703-727, 1964.

[31] H. Brenner, "Effect of finite boundaries on the Stokes resistance of an arbitrary particle" *Journal of Fluid Mechanics*, 12, pp.35-48, 1962.

[32] J. T. Padding and W. J. Briels, "Translational and rotational friction on a colloidal rod near a wall," *The Journal of Chemical Physics*, 132, pp. 054511-1:8, 2010.

[33] H. Faxen, "The velocity of two spheres that fall under the influence of gravity in a viscous fluid," (Translated title) *Zeitschrift für Angewandte Mathematik und Mechanik*, 7, pp.79-80, 1927.

[34] M. Stimson and G. B. Jeffrey, "The motion of two sheres in a viscous fluid," *Proceedings of the Royal Society*, A111, pp. 110-116, 1926.

[35] J. Happel and H. Brenner, *Low Reynolds Number Hydrodynamics*, Englewood Cliffs, Prentice Hall, 1965.

[36] H. Brenner, "Coupling between the translational and rotational Brownian motions of rigid particles of arbitrary shape," *Journal of Colloid and Interface Science*, 23, pp. 407-436, 1967.

[37] All references to commercial products in this paper are provided only to document how results have been obtained. Their identification does not imply recommendation or endorsement by NIST.

[38] The time T_{ss} required to reach steady state is given by $T_{ss} = (\frac{log(100)}{\pi^2}) \cdot \frac{\rho h^2}{\mu}$, where h and ρ are the height of the channel and the density of the fluid respectively as derived in
N. A. Patankar and H. H. Hu. "Numerical simulation of electro-osmotic flow," *Analytical Chemistry*, 70, 9, pp. 1870-1881, September 1998.
T_{ss} equals 0.32 ms in the device which is much less than the control update interval of 10 ms that is typically used in our flow control device. No discernible time lag in fluid actuation was observed in previous, position control experiments [5] in our group. Hence we assume that the flow velocity reaches steady state as soon as the voltages are applied.

[39] G. Strang, *Linear Algebra and its Applications*, Pacific Grove, California, Brooks Cole, 1988.

[40] H. Brenner, "Orientation-space boundary layers in problems of rotational diffusion and convection at large rotary Peclet numbers," *Journal of Colloid and Interface Science*, 34, 1, pp. 103-125, 1970.

[41] D.T. Gillespie, "The mathematics of Brownian motion and Johnson Noise," *American Journal of Physics*, 64, 3, March 1996, pp.225-240.

[42] D. R. Lide (Editor-in-chief) *CRC handbook of Chemistry and Physics*, CRC press, Ed. 90, 2009.

[43] A computational time of 3.5 ms, using MATLAB (www.mathworks.com) [37], was required for previous experiments that implemented position control of spherical particles. This includes

the time needed to estimate the particle position as well as the time needed to compute the control voltages. The frame rate of the Pike camera from Allied Vision Technologies (www.alliedvisiontec.com) [37] is 200 Hz at full resolution. Thus the total feedback loop time of 8.5 ms is within the 10 ms time assumed here.

[44] L. Sonneborn and F. Van Vleck, "The Bang-Bang principle for Linear Control Systems," *SIAM Journal On Control*,2, pp.151-159, 1965.

[45] F. Liu, B. Yi, D. Xing, J. Yu, and H. Zhang, "Nafion/PTFE composite membranes for fuel cell applications," *Journal of Membrane Science*, 212, 1-2, pp. 213-223, February 2003.

[46] Y. Han, A. M. Alsayed, M. Nobili, J. Zhang, T.C. Lubensky, A.G. Yodh "Brownian motion of an ellipsoid," *Science*, 314, pp. 626-630, October 2006.

[47] A. Sellier , "A note on the electrophoresis of a uniformly charged particle," *Quarterly Journal of Mathematics and Applied Mechanics* 55, 4, pp.561-572, 2002.

[48] N. I. Gamayunov, V. A. Murtsovkin, and A. S. Dukhin, "Pair Interaction of Particles in electric field - 1. Features of hydrodynamic interactions of polarized particles," Colloid Journal USSR, 48, pp.197-203, 1986.

[49] T. M. Squires and M. Z. Bazant, "Breaking symmetries in induced-charge electro-osmosis and electrophoresis," *Journal of Fluid Mechanics*, 560, pp.65-101, 2006.

[50] E. Yariv, "Induced -charge electrophoresis of nonspherical particles," *Physics of Fluids*, 17, 051702, 2005.

[51] D. Saintillan, E. Darve, and E. S. G. Shaqfeh, "Hydrodynamic Interactions in the induced-charge electrophoresis of colloidal rod suspensions," *Journal of Fluid Mechanics*, 563, pp.223-259, 2006.

[52] K. Rose, J. A. Meier, G. M. Dougherty, and J. G. Santiago "Rotational electrophoresis of striped metallic microrods," *Physical Review E*, 75, 011503, 2007.